Disentangling hole subbands dispersion in Si(111): In- and out-of-plane effective masses and anisotropy

Sakura Nishino Takeda,* Atsushi Kuwako, Masahiro Nishide, and Hiroshi Daimon
Graduate school of Materials Science, Nara Institute of Science and Technology (NAIST), 8916-5, Ikoma, Nara, 630-0192 Japan
(Received 10 October 2013; revised manuscript received 3 February 2016; published 16 March 2016)

We disentangle complex Si(111) hole subbands dispersion obtained by angle-resolved photoelectron spectroscopy and classify the subbands into three valence components. Through this procedure, quantum numbers and in-plane effective masses of the subbands are determined. The in-plane effective masses are close to the effective masses of a Si bulk valence band obtained by the first-principles calculations. Out-of-plane effective masses are obtained within the framework of triangular potential approximation. The results are compared to the reported theoretical results examining the validity of the theory. Energy separations of the subbands, order of the subbands, and out-of-plane effective masses are found to be basically in good agreement with the theoretical results.

DOI: 10.1103/PhysRevB.93.125418

I. INTRODUCTION

One strategy to enhance the performance speed of the metal-oxide-semiconductor field effect transistor (MOSFET) is to enhance carrier mobility in the channel region [1,2]. Among the various parameters affecting the carrier mobility, the effective mass of carrier is the most fundamental factor which determines the ultimate carrier velocity in an ideal condition. Importance of the effective mass further increases in advanced MOSFET with the channel length shorter than the carrier mean free path, which is in an order of 10 nm in silicon, because ballistic carrier transport is expected. Band effective mass directly relates to the second derivative of the electron band dispersion curve which is basically specific to both semiconductor material and its crystallographic orientation. In the channels in MOSFETs, carriers are confined in an inversion layer (IL) and quantized in perpendicular to the interface. The band structure is transformed into multiplet "subbands" by the confinement. The determination of the subband dispersion curve leads to the determination of the crystallographic-orientation-specific carrier effective mass in IL. From this point of view, the subband dispersions of both electrons and holes have been theoretically studied extensively [3–6]. However, compared to the electron subbands, theoretical determination of the hole subband (HSB) dispersion is still a challenging problem due to the complicated nature of the valence bands. Thus, experimental determination of HSB dispersion will provide a better perspective on mobility enhancement technology.

We have recently developed a method to observe the HSBs dispersion in p-type ILs directly using angle-resolved photoelectron spectroscopy (ARPES) [7]. In this method, p-type ILs are made by surface structures which store sufficient electrons necessary to induce strong band bending. Using this method, HSB dispersions in Si(111) and Si(001) p-type ILs have been reported so far [7–10]. Through these studies we showed complicated HSB dispersion due to both the interaction between adjacent HSBs and discontinuity of dispersion lines arising from the variation of the photoelectron intensity [10]. The top of the valence band of bulk silicon is composed of three $3p$ electrons. At the Γ point they are orthogonalized into heavy hole (HH), light hole (LH), and split-off (SO) bands. Within the framework of the standard Hamiltonian which describes valence electrons in ILs [11], HH, LH, and SO are still an orthogonalized basis set at the Γ point. Then the observed HSBs should be classified into these three components. This classification is very important to interpret the observed HSBs further. It is because a series of quantum numbers have to be assigned to the HSBs classified into the same component. Without appropriate classification, we cannot assign quantum numbers to the observed HSBs. However, it has been difficult to classify the observed HSBs into each component due to the complexity of the dispersion structure.

Our aim in this paper is to give quantum numbers to the observed HSBs in Si(111) IL and draw HSBs dispersion structure which is capable of being compared with theoretical results. To achieve this, we first discuss the validity of the parabolic fitting to the HSBs dispersion structure. Then we disentangle the HSBs dispersion curves into different groups using parabolic fitting. In-plane effective masses for each HSB are obtained through the fitting. Based on their in-plane effective mass, we classify HSBs into three groups and give them the quantum numbers. The classified groups are examined whether they are compatible with the triangular potential-well approximation (TPA) [15]. Within the framework of TPA, effective masses of HSB along perpendicular to the interface are obtained, too. Finally, the obtained results are compared with the available theoretical results [5,6].

II. EXPERIMENT

The sample preparation and the ARPES measurement were done in a UHV chamber [16]. For photoelectron excitation, monochromatized VUV light ($h\nu = 21.2$ eV) from a He discharge lamp (VG Scienta AB, VUV5000) was used. Photoelectron energy spectra were measured by a concentric hemispherical electron energy analyzer (VG Scienta AB, SES2002). Momentum (or wave number k) scan was achieved through scanning the photoelectron emission angle θ from

*sakura@ms.naist.jp

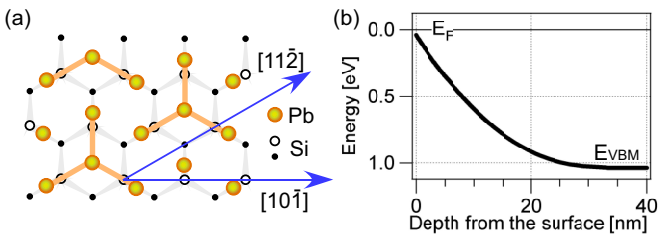

FIG. 1. (a) Structure model of Si(111)$\sqrt{3} \times \sqrt{3}$-Pb (SIC) [12–14]. (b) Band bending curve of the sample in this study [10].

the sample normal both by using the finite acceptance angle ($\pm 6^\circ$) of the analyzer and by rotating the sample. θ is converted to k using the relation $k = (\sqrt{2m_0}/\hbar)\sqrt{E_k}\sin\theta$. m_0 is the free electron mass and E_k is the kinetic energy of the photoelectrons. The in-plane orientation of the wave vector k was changed by sample rotation around the sample normal. The sample was at room temperature during ARPES measurements.

We employed Si(111)$\sqrt{3} \times \sqrt{3}$-Pb (striped incommensurate: SIC) [12–14,17] as the surface structure to induce strong band bending. Si(111)$\sqrt{3} \times \sqrt{3}$-Pb (SIC) can accommodate a large number of electrons as surface carrier in its electronic states owing to its large density of surface states, enough to induce a strong band bending. The surface structure affects the Si subband dispersion only if it has surface states near the subbands in the E-k space (and also in the real space). In the case of $\sqrt{3} \times \sqrt{3}$ surface states, there are no such states around the region of interest in the E-k space [18]. So we can exclude the effect of surface states on subbands in the case here. The substrate was a piece of Si(111) wafer with a carrier concentration of 5×10^{18} cm^{-3}. The surface structure was monitored by RHEED during the sample preparation. The sample surface was cleaned in the UHV chamber by flash annealing with direct current heating. Pb was deposited on the heated Si(111) 7×7 clean surface until the surface structure converted to Si(111)$\sqrt{3} \times \sqrt{3}$-Pb (SIC) [13]. A schematic model of the atomic structure of Si(111)$\sqrt{3} \times \sqrt{3}$-Pb (SIC) is shown in Fig. 1(a) [12,14,17]. The Pb coverage of Si(111)$\sqrt{3} \times \sqrt{3}$-Pb (SIC) is reported to be 1.33 monolayer (ML). The shape of the band bending induced by Si(111)$\sqrt{3} \times \sqrt{3}$-Pb (SIC) is shown in Fig. 1(b). The potential curve was obtained by solving Poisson's equation [19] using the surface boundary condition given by the Si $3p$ peak shift [10]. There are two high-symmetry in-plane orientations, [11$\bar{2}$] and [10$\bar{1}$], on the Si(111) surface as shown in Fig. 1(a). In this article the dispersion structures of HSBs along these two orientations are investigated.

III. RESULTS AND DISCUSSION

A. Anisotropy and in-plane mass

Figure 2 shows ARPES intensity maps in energy (E)–momentum (k) space, which corresponds to the band dispersion diagram, along the two symmetric in-plane orientations of Si(111)$\sqrt{3} \times \sqrt{3}$-Pb (SIC) surface. Multiplet dispersion curves characteristic to HSBs confined in the IL are observed in both directions. The fundamental HSB ($n = 0$) locates at around 0.15 eV at $\bar{\Gamma}$ point in both Figs. 2(a) and 2(b). In the raw photoelectron energy distribution curves (EDC) shown in Fig. 3(a), they appear as prominent peaks labeled a. HSBs with higher indices appear at around 0.30, 0.50, and 0.65 eV at the $\bar{\Gamma}$ point in the dispersion map along [11$\bar{2}$]. They correspond to photoelectron peaks b, e, and f in Fig. 3(a). In the map along [10$\bar{1}$], besides these HSBs, additional HSBs appear at 0.35 eV (peak c) and 0.45 eV (peak d). Because the energy levels of HSBs at the $\bar{\Gamma}$ point should be identical in the band dispersions measured along any direction, this inconsistency should be a consequence of a variation of photoelectron intensity probably due to the photoelectron matrix element effect [20]. This has a severe impact on the analysis of HSB because one needs to know the energy levels of all the HSBs at the $\bar{\Gamma}$ point to give the collect quantum numbers for each energy level without

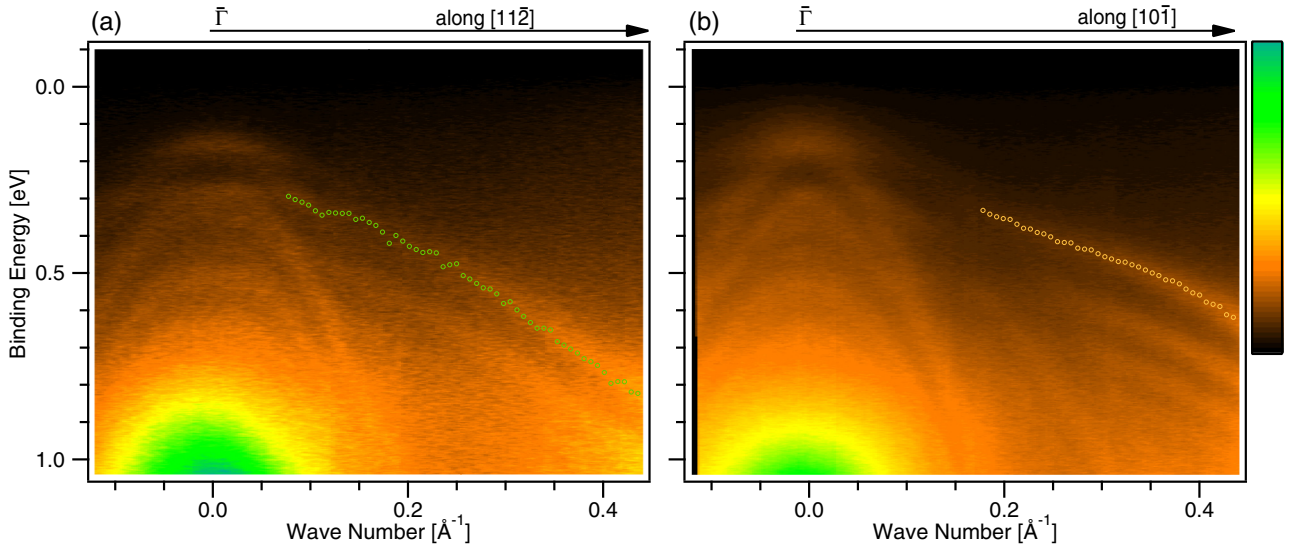

FIG. 2. ARPES photoelectron intensity maps of Si(111)$\sqrt{3} \times \sqrt{3}$-Pb (SIC) along (a) [11$\bar{2}$] and (b) [10$\bar{1}$]. The photoelectron intensities are represented using different colors as shown by the color bar on the right side.

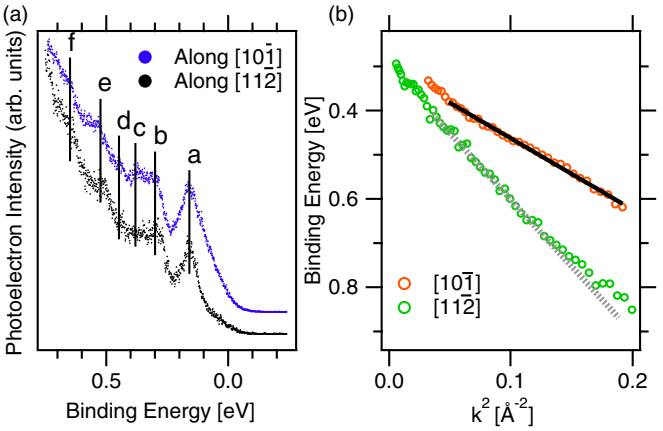

FIG. 3. (a) Photoelectron spectra at the $\bar{\Gamma}$ point of Si(111)$\sqrt{3}\times\sqrt{3}$-Pb (SIC) in the measurements along [11$\bar{2}$] [Fig. 2(a)] and [10$\bar{1}$] [Fig. 2(b)]. (b) Dispersion curves obtained from ARPES intensity maps (Fig. 2) are plotted against k^2.

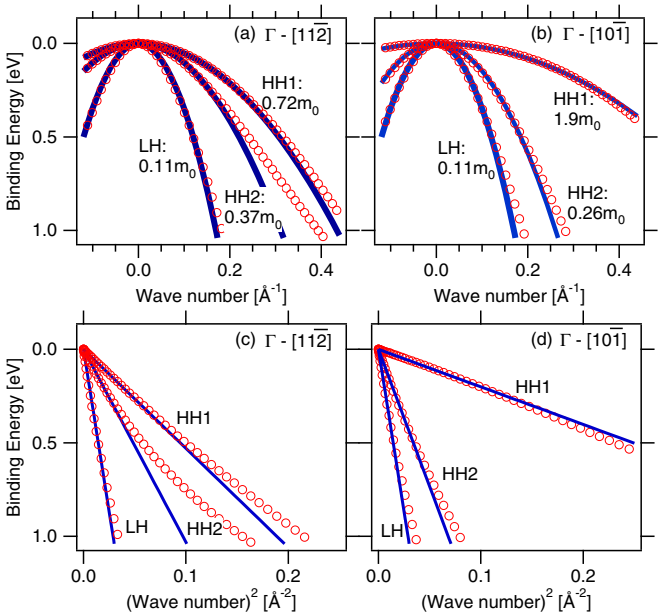

FIG. 4. Valence band dispersions of bulk Si (red circles) by the first-principles calculations along (a) [11$\bar{2}$] and (b) [10$\bar{1}$] directions. Blue lines are parabolic curves obtained by fitting the result of the first-principles calculations. Binding energy at the valence band maximum is set to 0 eV. Effective masses corresponding to these parabolic curves are indicated in the figure. The same dispersion structures are plotted against k^2 in (c) and (d) to see the parabolicity.

ambiguity. The next part of this paper is devoted to construct a method for the correct indexing. The strategy is as follows.

The apparent dispersion of HSBs (Fig. 2) consists of several segments of the subbands. Thus, the whole HSBs dispersion can be restored by fitting an appropriate function to the visible segments. Within the $k\cdot p$ approximation scheme [21], the bulk valence bands around the $\bar{\Gamma}$ point are expressed as quadratic functions. Though interactions between adjacent HSBs modifies the shape of the HSBs dispersion different from the quadratic functions, such interactions work only in the vicinity of the crossing points. Thus, except for the vicinity of the crossing points of HSBs [22], where the strong interactions take place, the HSBs should be in their own parabolic shapes. In this point of view, we chose quadratic functions to restore the subbands. Nevertheless, this idea is not always valid as seen in Fig. 3(b) in which the heaviest HSBs in both directions are plotted against k^2. The figure shows that the dispersion of heavy HSB is linear against k^2 only in the case of [10$\bar{1}$]. The heavy HSB along [11$\bar{2}$] deviates from the linear line. The HSBs along [11$\bar{2}$] direction is not in parabolic shape.

To see whether this nature originates in the bulk valence band structure or not, we examined parabolicity of the Si bulk valence bands obtained by the first-principles calculations [23] as shown in Figs. 4(a) and 4(b). In the figure the calculated band dispersion is shown together with the parabolic curves obtained by fitting to the bands around the $\bar{\Gamma}$ point. The bands are named as HH1, HH2, and LH in order of decreasing in-plane effective mass. As seen in the figure, the dispersion curves are parabolic in both directions at least in the vicinity of the $\bar{\Gamma}$ point. The effective masses obtained from these parabolic curves are indicated in the figure. The bands start to deviate from the parabolic curves at higher wave numbers. The deviation point and the amount of deviation depends on each band. HH1 along [10$\bar{1}$] is close to parabolic curvature up to 0.4 Å^{-1}. HH2 and LH along [10$\bar{1}$] direction and LH1 along [11$\bar{2}$] have minor deviation from the parabolic curves up to the binding energy of 1.0 eV from the valence band top. Comparing to these bands, HH2 along [11$\bar{2}$] deviates from the parabolic bands significantly even in the small wave number region. All calculated bands have a tendency to have effective mass heavier than the corresponding parabolic curves after the deviation points. To see the parabolicity more, the bands are plotted against k^2 in Figs. 4(c) and 4(d). It is clear that HH1 and HH2 along [11$\bar{2}$] are not linear against k^2.

This suggests that the nonparabolic character of the heavy HSB along [11$\bar{2}$] observed by ARPES originates in the nature of the Si bulk valence band. We concluded from these results that the above strategy, restoring HSB structure using parabolic band fitting, is only valid for the dispersion along [10$\bar{1}$] direction.

It is worth noting here that the above results are inconsistent with simple $k\cdot p$ approximation. In the case of the basic $k\cdot p$ approximation, the dispersion relation of the bulk valence band is expressed as

$$E_{\mathrm{LH}}^{\mathrm{HH}}(\boldsymbol{k}) = Ak^2 \pm \left[B^2k^4 + C^2\left(k_x^2k_y^2 + k_y^2k_z^2 + k_z^2k_x^2\right)\right]^{1/2}, \quad (1)$$

$$E_{\mathrm{SO}}(\boldsymbol{k}) = -\Delta_{\mathrm{SO}} + Ak^2. \quad (2)$$

A, B, and C are the parameters determined to reproduce the result of the cyclotron resonance on Si valence bands. $-\Delta_{\mathrm{SO}}$ is split-off energy and 44 meV for silicon. By substituting $\boldsymbol{k} = \frac{1}{\sqrt{6}}(k,k,-2k)$ for [11$\bar{2}$] direction and $\boldsymbol{k} = \frac{1}{\sqrt{2}}(k,0,-k)$ for [10$\bar{1}$] direction, one gets the same expression for the dispersion relation of HH and LH in both directions,

$$E(\boldsymbol{k}) = \left[A \pm \left(B^2 + \tfrac{1}{4}C^2\right)^{1/2}\right]k^2. \quad (3)$$

The effective mass m^* is obtained by setting the coefficient of k^2 in Eq. (3) equal to $\hbar^2/2m^*$. Because the E-k relations in [11$\bar{2}$] and [10$\bar{1}$] directions are expressed by the identical

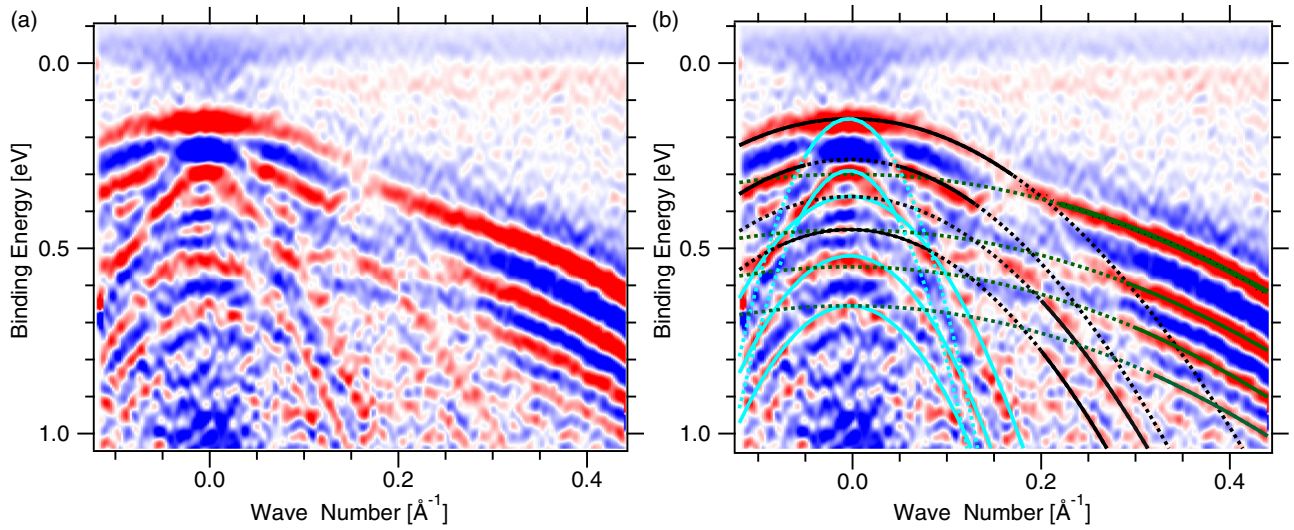

FIG. 5. (a) ARPES second-derivative intensity map of Si(111)$\sqrt{3} \times \sqrt{3}$-Pb (SIC) along [10$\bar{1}$]. Red corresponds to the peaks in the photoelectron spectra where electronic states exist. (b) Parabolic curves obtained by fitting to the observed HSB dispersion structure along [10$\bar{1}$] are overlaid on the ARPES second-derivative intensity map shown in (a). The solid lines indicate the fitted segments and the dashed lines are the rest of the parabolic curves. Green, black, and blue lines indicate v1-n, v2-n, and v3-n, respectively.

equation, the simple $k \cdot p$ approximation gives an identical effective mass for [11$\bar{2}$] and [10$\bar{1}$] directions in contrast to the HSB dispersion experimentally obtained in this work and the bulk dispersions obtained by the first-principles calculations shown above. Using $A = -4.29$, $B = 0.68$, and $C = 4.87$ in $\hbar^2/2m_0$ unit [24], the bulk effective masses in both directions are obtained to be $0.57m_0$, $0.15m_0$, and $0.23m_0$ for HH, LH, and SO. These values are similar to the effective masses from the first-principles calculations in [11$\bar{2}$] direction [Fig. 4(a)]. On the other hand, in [10$\bar{1}$] direction, the discrepancy of heavy hole mass obtained by the first-principles calculations ($1.9m_0$) and the $k \cdot p$ approximation reaches more than a factor of 3. $k \cdot p$ approximation is valid within a small energy region less than spin-orbit splitting energy (44 meV for Si) from the valence band top, whereas the energy region used to estimate the effective masses from the results of the first-principles calculations in this study is approximately 500 meV or more. Thus the discrepancy might be partially caused by the the difference of the targeting energy region in these calculation methods. Nevertheless, we remind to the readers that isotropic valence band dispersion of Si in (111) plane obtained by the simple $k \cdot p$ approximation does not match the observed HSB dispersion nor the results of the first-principles calculations. Furthermore, effective mass along [10$\bar{1}$] obtained by the $k \cdot p$ approximation differ significantly from those obtained by the first-principles calculations. More accurate framework such as use of increased number of basis set [25] would be more appropriate to describe Si valence bands quantitatively using $k \cdot p$ approximations.

Based on the above findings, fragments of HSBs along [10$\bar{1}$] direction are fitted by parabolic curves expressed as

$$E(k) = \frac{\hbar^2}{2m^*}k^2 + E_n. \quad (4)$$

Here the fitting parameters are in-plane effective mass m^* and binding energy at the $\bar{\Gamma}$ point E_n. The result of the fitting is shown in Fig. 5. The regions used to the fitting are indicated by solid lines and the rest of the parabolic curves are indicated by the dashed lines. The obtained fitting parameters are summarized in Table I. The parabolic curves are categorized into three groups in terms of the in-plane effective mass as expressed by different colors in the figure. We named them as v1 (green), v2 (black), and v3 (blue). HSBs within each group are expressed as v1-n, v2-n, and v3-n using the quantum number n starting from 0 for the HSB closest to the E_F.

B. Out-of-plane mass

Once the quantum numbers are given to each HSB, we can compare the experimental result with TPA. In TPA the confinement potential curve is approximated to a linear line.

TABLE I. In-plane effective mass m^* and E_n obtained from parabolic curves fitted to HSBs along [10$\bar{1}$] shown in Fig. 5(b).

[10$\bar{1}$]	m^* (m_0)	E_n (eV)
v1-0	2.4 ± 0.3	0.29 ± 0.02
v1-1	2.09 ± 0.03	0.432 ± 0.004
v1-2	2.09 ± 0.04	0.551 ± 0.005
v1-3	2.12 ± 0.05	0.659 ± 0.006
v2-0	0.78 ± 0.03	0.156 ± 0.002
v2-1	0.54 ± 0.02	0.268 ± 0.002
v2-2	0.60 ± 0.03	0.365 ± 0.005
v2-3	0.48 ± 0.02	0.450 ± 0.003
v3-0	0.08 ± 0.01	0.150 ± 0.008
v3-1	0.098 ± 0.007	0.300 ± 0.005
v3-2	0.18 ± 0.02	0.397 ± 0.003
v3-3	0.18 ± 0.00	0.538 ± 0.003
v3-4	0.17 ± 0.00	0.662 ± 0.003

As seen in the shape of the IL shown in Fig. 1, this is reasonable between $z = 0$ and approximately 10 nm in our sample. Within the TPA, one can obtain the quantized energy levels at the $\bar{\Gamma}$ point (E_n) analytically. The energy levels obtained by TPA are expressed in the form

$$E_n = \frac{1}{(2m_z^*)^{1/3}}(\hbar e F_s)^{2/3}\gamma_n + V_0, \tag{5}$$

m_z^* is the HSB effective mass along z ([111]) direction, V_0 is the confinement potential energy at $z = 0$, and F_s is the electric field which makes the linear confinement potential. γ_n is the value where the Airy function becomes 0, i.e., $\gamma_0 = 2.338$, $\gamma_1 = 4.088$, $\gamma_2 = 5.521$, and $\gamma_3 = 6.787$ [26]. Because there is an ambiguity in m_z^*, we treat the coefficient of the γ_n as a fitting parameter A:

$$A = \frac{1}{(2m_z^*)^{1/3}}(\hbar e F_s)^{2/3}. \tag{6}$$

Now it is clear that E_n is expressed as a linear function of γ_n with slope A and intercept V_0,

$$E_n = A\gamma_n + V_0. \tag{7}$$

Using Eq. (7) we examined whether the experimentally obtained sets of E_n follow this description or not by plotting the experimentally obtained E_n shown in Table I against γ_n for each group. The result is shown in Fig. 6. Here we can see that the sets of E_n of v1 and v2 are very well fitted by straight lines. A rough estimate of the validity of the straight-line approximation to the band bending curve shown in Fig. 1(b) indicates that the TPA is valid only at low energies (up to 0.5 eV). So the excellent linear behavior of v1 up to 0.65 eV is beyond our expectation. The obtained fitting parameters

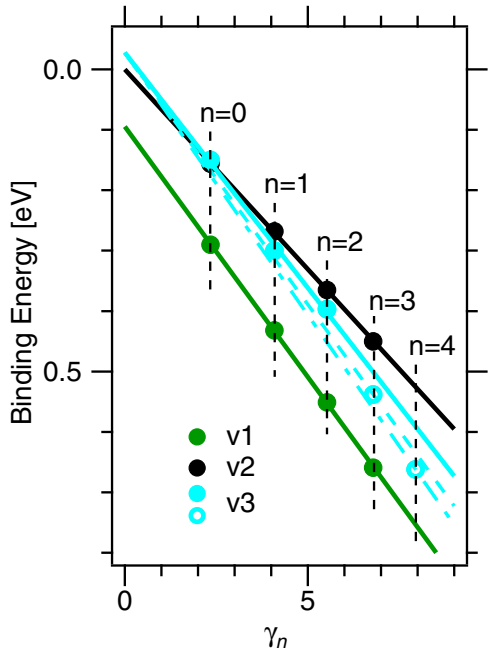

FIG. 6. E_n shown in Table I are plotted against γ_n. v1, v2, and v3 groups are presented by different colors corresponding to the parabolic curves in Fig. 5. Lines indicate the result of fittings for each group based on the TPA approximation.

TABLE II. A and V_0 in Eq. (7) obtained by fitting E_n and m_z^*. The values for v3-3 and v3-4 are derived from lines connecting each point and V_0 obtained by fitting v3-0, -1, and -2.

	A (eV)	V_0 (eV)	m_z^* (m_0)
v1	0.083 ± 0.0007	0.095 ± 0.003	0.33 ± 0.01
v2	0.066 ± 0.0006	0.000 ± 0.003	0.65 ± 0.02
v3	0.078 ± 0.005	−0.028 ± 0.021	0.40 ± 0.08
v3-3	0.083	–	0.34
v3-4	0.087	–	0.28 ± 0.05

A and V_0 are summarized in Table II. Furthermore, using $F_s = 0.07$ eV/nm obtained from Fig. 1(b) and using these values of A, one can get m_z^* for each group from Eq. (6). They are also summarized in Table II. The linear relationship means that each v1-n and v2-n subbands group has a single out-of plane effective mass irrespective of quantum number n. The fundamental HSB, v2, has heaviest m_z^*. This is in good agreement with one of the main characteristics of TPA derived from Eq. (5). The $k \cdot p$ effective masses of bulk valence bands along [111] direction are $0.72m_0$, $0.14m_0$, and $0.23m_0$ for HH, LH, and SO, respectively. They are of the same order as the m_z^* for v1 and v2 obtained through the above analysis. On the other hand, bulk effective masses derived from dispersion relations along [111] direction by the first-principles calculations are $2.5m_0$ and $0.37m_0$ for HH (doubly degenerated) and LH as shown in Fig. 7. They are much heavier than $k \cdot p$ bulk masses and m_z^* for HSBs obtained in this work. This discrepancy may be again attributed to the difference in the targeting energy region. V_0 has been already obtained to be 0.04 eV through the analysis of Si $3p$ peak shift [10] as shown in Fig. 1(b). V_0 for group v2 obtained through the analysis here (0.00 eV) is in good agreement with the value obtained by Si $3p$ peak shift. The similarity of the values of V_0 obtained by two independent methods supports the validity of our arguments here. In the case of v1, V_0 is approximately 100 meV higher than the V_0 of v2. Considering that the bulk SO band maximum locates at higher binding energy by Δ_{SO} (44 meV) than that of the bulk

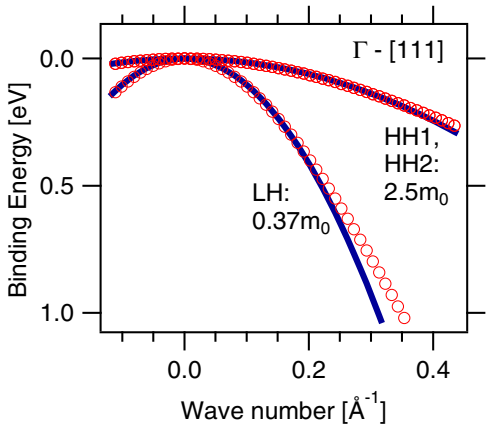

FIG. 7. Valence band dispersions of bulk Si along [111] direction from the Γ point. Red circles are obtained by the first-principles calculations and the blue lines are the fitting using parabolic curves.

HH and LH, the difference of 100 meV would suggest that HH1 has the bulk SO character around the $\bar{\Gamma}$ point.

The E_n of v3 group, on the other hand, are not fitted by a single straight line. In Fig. 6 only the first three energy levels, v3-0, v3-1, and v3-2, are on the solid line. Parameters A, V_0, and m_z^* for LH listed in Table II are obtained by fitting them. v3-3 and v3-4 are obviously away from the line.

At higher binding energies, where the IL potential curve starts to deviate from the linear potential line of TPA, TPA would no longer be a suitable approximation. However, because the confinement width of the real IL potential becomes wider than the TPA line at higher binding energy, a necessary correction to the TPA energy levels to compensate for the error of the TPA potential line shifts them to lower binding energy. The measured v3-3 and v3-4, on the other hand, appear at higher binding energies than the result of TPA shown as the line in Fig. 6. So the deviation of the TPA straight line from the real IL potential curve does not explain the strange behavior of v3-3 and v3-4.

Within the framework of TPA, this situation means that v3-n group is not described by a common m_z^* in contrast to v1-n and v2-n groups. Namely, the v3-3 and v3-4 have their own m_z^*. Their m_z^* are obtained through the lines connecting V_0 obtained by the fitting of v3 and v3-3 or v3-4 as shown by dashed lines in Fig. 6. The result listed in Table II indicates m_z^* decreases with increasing n. Why only does the v3-n group have different m_z^* depending on n? A recent study [18] on a Si(111)Pb-$\sqrt{7} \times \sqrt{3}$ system proposed that the surface states repulsively interact only with the LH band, but not with the HH band, in Si due to the band symmetry. Si(111)Pb-$\sqrt{7} \times \sqrt{3}$ is a low temperature phase of Si(111)$\sqrt{3} \times \sqrt{3}$-Pb (hexagonal incommensurate: HIC), which is formed at slightly lower Pb coverage than Si(111)$\sqrt{3} \times \sqrt{3}$-Pb (SIC) [13,27]. In the case of Si(111)$\sqrt{3} \times \sqrt{3}$-Pb (SIC), however, the existence of such surface states has been denied [18]. Thus an effect from the surface states is unlikely. The reason will be clarified by measuring the HSB under other surface structures.

C. Comparison with theoretical results

HSBs in Si(111) ILs have been calculated by Fischetti *et al.* [5] and Donetti *et al.* [6] using a six-band $k \cdot p$ and TPA. According to Fig. 3 in Ref. [5], the order of the HSB energy levels at the surface field of $F_s = 0.07$ eV/nm is HH, LH, HH, LH, and SO from the fundamental HSB. The labeling of the subbands in their article is from the in-plane mass too. This order is the same with our result if one assigns v1 and v2 to be SO and HH as discussed above. Furthermore, the energy splittings of each HSB level at the $\bar{\Gamma}$ point are in good agreement between this work and Fig. 3 in Ref. [5]. For example, energy splitting between v2-0 and v2-1 at the $\bar{\Gamma}$ point is 0.11 eV in our data, and the energy splitting between the fundamental HH and the first excited HH is 0.11 eV too in their calculations at $F_s = 0.07$ eV/nm. This coincidence ensures that the method employed in Ref. [5] to calculate HSB dispersion well describes the real HSBs in Si IL. In the case of Ref. [6], the order of the HSB energy levels at the surface field of $F_s = 0.07$ eV/nm is HH, LH, HH, LH, and LH. Though the first four HSB is the same with us and Ref. [5], the ground SO subband seems to appear at much higher binding energy than us. The energy splitting between the fundamental and the first excited HH is 0.12 eV, which is close enough to our results. In Ref. [6], m_z^* are calculated as well. According to Fig. 1(f) in Ref. [6], the m_z^* of HH, LH, and SO subbands at the surface field of $F_s = 0.07$ eV/nm are approximately $0.7m_0$, $0.4m_0$, and $0.06m_0$, respectively. The values of m_z^* for HH and LH are in good agreement with the experimental values here. In the case of SO, our result ($0.33m_0$) is five times larger than Ref. [6]. This discrepancy probably relates to the discrepancy in the order of the HSB energy levels mentioned above.

IV. CONCLUSIONS

As a conclusion, we disentangled HSBs dispersion in Si(111) p-type IL observed by ARPES. Though the observed HSBs were an assembly of the fragments of the HSBs, we restored the complete HSBs dispersion structure along [10$\bar{1}$] direction using a parabolic dispersion relation. The validity of the use of a parabolic dispersion relation was confirmed through the first-principles calculations. Quantum numbers were assigned to all restored HSBs and their in-plane effective masses were obtained. The HSBs energy levels of HH1 (SO) and HH2 (HH) at the $\bar{\Gamma}$ point were found to be well described by TPA. On the other hand, LHs were not described by TPA. We attributed it to the interaction of LHs with surface states. Within the framework of TPA, out-of-plane effective masses of HSBs were obtained. We found the energy splittings of the HSB calculated using six-band $k \cdot p$ and TPA excellently reproduce our results.

We believe that the analysis method described here is useful to analyze experimentally obtained HSBs, which is complicated due to the interactions of the three components in contrast to the electron subbands, which is composed of one component. Experimentally, the condition of the photoelectron excitation process has to be changed to observe all the HSB structures. ARPES using linearly polarized light as incident light and changing the direction of the polarization vector of the light is required to see the entire HSBs dispersion, which will be our next task. So far experimental studies on HSBs have been mainly through the mobility measurements. Thus theoretical studies as a counterpart of the experiments have focused on the mobilities derived from HSBs. Though the direct observation on HSB dispersion have been started recently using ARPES, the characterization of the observed HSB dispersion, such as assignment of quantum numbers and determination of effective mass of HSBs, had not succeeded so far. In this paper we showed such characterization is possible for the HSBs observed by ARPES. We hope that this study encourages future theoretical studies on HSBs dispersion as a counterpart of the experimental results.

ACKNOWLEDGMENTS

We would like to thank Professor Takeshi Inaoka (University of the Ryukyus) for valuable discussions. This work was supported by Semiconductor Technology Academic Research Center (STARC) and by JSPS KAKENHI Grants No. 24360018, No. 22540332, and No. 26105014.

[1] S.-i. Takagi, T. Mizuno, T. Tezuka, N. Sugiyama, S. Nakaharai, T. Numata, J. Koga, and K. Uchida, Solid State Electron. **49**, 684 (2005).
[2] T. Skotnicki, C. Fenouillet-Beranger, C. Gallon, F. Buf, S. Monfray, F. Payet, A. Pouydebasque, M. Szczap, A. Farcy, F. Arnaud, S. Clerc, M. Sellier, A. Cathignol, J. P. Schoellkopf, E. Perea, R. Ferrant, and H. Mingam, IEEE Trans. Electron Devices **55**, 96 (2008).
[3] M. V. Fischetti and S.-E. Laux, Phys. Rev. B **48**, 2244 (1993).
[4] J.-L. van der Steen, D. Esseni, P. Palestri, L. Selmi, and R. Hueting, IEEE Trans. Electron Devices **54**, 1843 (2007).
[5] M. V. Fischetti, Z. Ren, P. M. Solomon, M. Yang, and K. Rim, J. Appl. Phys. **94**, 1079 (2003).
[6] L. Donetti, F. Gámiz, S. Thomas, T. E. Whall, D. R. Leadley, P.-E. Hellström, G. Malm, and M. Östling, J. Appl. Phys. **110**, 063711 (2011).
[7] S. N. Takeda, N. Higashi, and H. Daimon, Phys. Rev. Lett. **94**, 037401 (2005).
[8] M. Morita, S. N. Takeda, M. Yoshikawa, A. Kuwako, Y. Kato, and H. Daimon, Appl. Surf. Sci. **254**, 7872 (2008).
[9] Y. Tanigawa, S. N. Takeda, M. Morita, T. Ohsugi, Y. Kato, H. Daimon, M. Yoshimaru, and T. Imamura, J. Surf. Sci. Nanotech. **7**, 641 (2009).
[10] S. N. Takeda, N. Higashi, and H. Daimon, Phys. Rev. B **82**, 035318 (2010).
[11] T. Ando, A. B. Fowler, and F. Stern, Rev. Mod. Phys. **54**, 437 (1982).
[12] L. Seehofer, G. Falkenberg, D. Daboul, and R.-L. Johnson, Phys. Rev. B **51**, 13503 (1995).
[13] K. Horikoshi, X. Tong, T. Nagao, and S. Hasegawa, Phys. Rev. B **60**, 13287 (1999).
[14] T.-L. Chan, C.-Z. Wang, M. Hupalo, M.-C. Tringides, Z.-Y. Lu, and K.-M. Ho, Phys. Rev. B **68**, 045410 (2003).
[15] F. Stern, Phys. Rev. B **5**, 4891 (1972).
[16] H. Yamatani, K. Hattori, T. Matsuta, T. Ito, T. Nohno, M. Hori, Y. Miyatake, S. Konno, T. Tanaka, Y. Hamada, H. Katagiri, M. Hibi, T. Miyai, M. Hashimoto, K. Kataoka, T. Tatsuta, A. N. Hattori, N. Higashi, M. Honda, N. Masunaga, H. Mino, S. Yasui, J. Nayeem, T. Shimizu, N. Takahashi, Y. Kato, C. Sakai, M. Yoshimura, S. N. Takeda, F. Matsui, and H. Daimon, Surf. Sci. **601**, 5284 (2007).
[17] T. Zhang, P. Cheng, W.-J. Li, Y.-J. Sun, G. Wang, X.-G. Zhu, K. He, L. Wang, X. Ma, X. Chen, Y. Wang, Y. Liu, H.-Q. Lin, J.-F. Jia, and Q.-K. Xue, Nat. Phys. **6**, 104 (2010).
[18] K. S. Kim, S. C. Jung, M. H. Kang, and H. W. Yeom, Phys. Rev. Lett. **104**, 246803 (2010).
[19] W. Mönch, *Semiconductor Surfaces and Interfaces* (Springer, Berlin, 1995).
[20] H. Daimon, S. Imada, H. Nishimoto, and S. Suga, J. Electron Spectrosc. Relat. Phenom. **76**, 487 (1995).
[21] C. Kittel, *Quantum Theory of Solids* (Wiley, New York, 1987).
[22] Y.-T. Hou and M.-F. Li, IEEE Trans. Electron Devices **48**, 2893 (2001).
[23] Y. Yamazaki, K. Shirai, and H. Katayama-Yoshida, Solid State Commun. **126**, 597 (2003).
[24] C. Kittel, *Introduction to Solid State Physics* (Wiley, New York, 1986).
[25] S. Richard, F. Aniel, and G. Fishman, Phys. Rev. B **72**, 245316 (2005).
[26] M. Abramowitz and I. Stegun, *Handbook of Mathematical Functions*, 9th ed., edited by M. Abramowitz and I. Stegun (Dover, New York, 1970).
[27] S. Stepanovsky, M. Yakes, V. Yeh, M. Hupalo, and M. Tringides, Surf. Sci. **600**, 1417 (2006).